

Comparison of measured and simulated motion of a scaled dragline excavation system

Jason Kyle, Mark Costello*

Department of Mechanical Engineering, Oregon State University, Corvallis, OR, 97331, United States

Received 8 August 2005; received in revised form 13 February 2006; accepted 21 February 2006

Abstract

Motion measurements obtained from a maneuvering 1/16-scale dragline excavation system using a six camera motion capture system are compared against motion predictions of the same scenario using a complex dragline excavation system simulation. The dynamic model includes motion of the bucket, spreader bar, hoist cluster, and drag cluster, along with flexible rope and chain segments including the hoist rope, drag rope, dump rope, hoist chains, and drag chains. In general, measured and simulated motions agree quite favorably. However, a consistent difference between the measurements and the simulation model is damping of oscillations, where it is noticed that measurement data tend to damp more rapidly than simulation model results.

© 2006 Elsevier Ltd. All rights reserved.

Keywords: Dragline; Excavator; Simulation; Validation; Dynamic model; Motion capture

1. Introduction

Surface mining extracts underground resources that reside close to the Earth's surface and involves a process of moving soil covering the resource to a storage location and subsequently removing the resource. Overburden, defined as soil covering a resource, is most efficiently moved by a dragline excavation system in many surface mining scenarios. As shown in Figs. 1 and 2, a dragline excavation system is fitted with an open bucket supported above by a cable hanging from the end of a long boom. The bucket is dragged along the ground by a cable until it is filled with earth, which is then dumped elsewhere. Draglines are used primarily in high-volume overburden removal and excavation of deep holes. The complete system contains many dynamic components, including the excavator, boom, bucket, spreader bar, drag coupler, hoist coupler, hoist chains, drag chains, hoist rope, drag rope, and dump rope. The bucket is indirectly controlled by an operator in the excavator through rotation of the boom about a vertical axis and payout and windup of the hoist and drag ropes. Lowering and lifting of the bucket is accomplished mainly with the hoist rope, while longitudinal motion of the bucket is accomplished mainly through the drag rope.

Physically, dragline excavator systems are typically very large-scale devices. Common medium-sized dragline excavation systems weigh 500 metric tons with a bucket capable of moving 23 m³ of material in a single cycle. An average-sized boom is 91 m long. Not only are dragline excavation systems physically big, they are equally large from

* Corresponding author.

E-mail address: mark.costello@comcast.net (M. Costello).

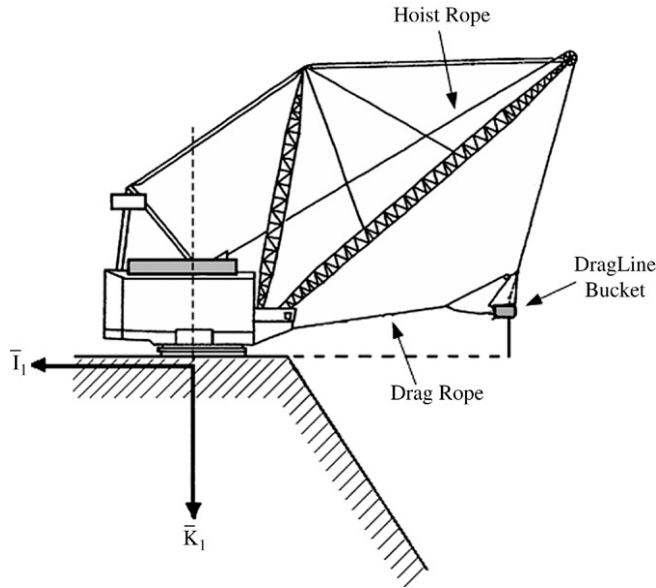


Fig. 1. Dragline excavation system schematic.

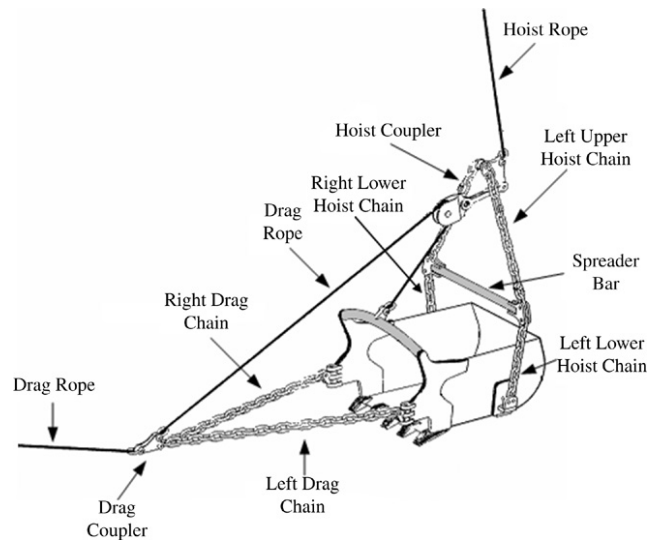


Fig. 2. Dragline bucket schematic.

an economic perspective. Surface mining at large sites is big business, with high revenue opportunities as well as high operating costs. In many surface mining operations, removal of overburden dominates the cost side of operating a mine. Relatively small improvements in dragline excavator system performance such as cycle time, bucket capacity, working envelope, component life, etc. can map into sizeable economic gains for the mine operator.

For slowly operating dragline excavation systems, static system models provide a satisfactory estimate of component loads that is utilized in structural sizing of system components. Static system models also provide bucket position and orientation information for various hoist and drag rope lengths and various bucket riggings that are useful for site excavation planning. In cases where relatively rapid maneuvering of the dragline system is encountered, the use of a dynamic dragline excavation model is more appropriate for estimating bucket orientation excursions and maximum loads on different components.

Several research groups have developed dragline excavation system models at various levels of sophistication for different analytical purposes. McCoy and Crowgey [1] investigated static and dynamic dragline bucket tightline control. Using simple geometric analysis, they constructed both static and dynamic tightline limits based on the length of the drag and hoist ropes, and subsequently used these limits as part of an anti-tightline control system. Haneman et al. [2] reported on dragline performance evaluations using physical modeling. Rigging geometry and bucket size were optimized using physical modeling and compared against field data. Rowlands and Just [3] documented experimental results on a dragline bucket digging and filling capability. They concluded that design changes to conventional dragline buckets can be made to improve performance by reducing filling times and dig energy consumption. Knight and Shanks [4] investigated dragline productivity improvements through short term monitoring. A productivity benefit of 2% was realized using a monitoring system that computes an optimized bucket rigging. Pathak et al. [5] generated a method to compute the working zone of a dragline bucket. A graphical approach for the determination of the bucket path profile of a standard dragline was indicated, considering the simple three-period duty cycle in each operation. Hainsworth et al. [6] used machine vision techniques to measure the location of a dragline bucket in space remotely. Using only a single camera, an image segmentation process is used to classify the bucket and to identify its position in the scene. Cleary, [7] investigated dragline bucket filling using a discrete element model to simulate the filling process. Ridley and Corke [8] developed a technique to estimate dragline bucket pose under gravity loading. Their model is based on static equilibrium of the loads on the different components of the system.

The intricate geometric arrangement of different dragline excavation system components, coupled to the fact that each component can significantly alter motion characteristics, leads to the necessity of employing a fairly complex dynamic simulation model to replicate physical behavior. In the work reported here, measured and simulation motion for an example 1/16-scale dragline excavation system are compared. Measurements are recorded with an optical motion capture system. The dynamic model includes three-dimensional (3-D) rigid body motion of the bucket, spreader bar, drag cluster, and hoist cluster, as well as flexible motion of all chains and ropes. A typical dig maneuver, without a bucket load, is presented in the comparison of results.

2. Dragline excavation system dynamic model

The dynamic event considered consists of the motion of a complete dragline excavation system. As shown in Figs. 1 and 2, the total system contains four rigid bodies and nine ropes. The rigid bodies include the bucket, spreader bar, hoist coupler, and drag coupler. The ropes include the drag rope, dump rope, hoist rope, left drag chain, left lower hoist chain, left upper hoist chain, right drag chain, right lower hoist chain, and right upper hoist chain. The surface of the ground is assumed to be a satisfactory inertial reference. As shown in Fig. 1, the inertial reference frame is a right-handed coordinate system defined with its origin on the ground surface located below the excavator at the point of azimuth rotation of the excavator. The \vec{I}_I and \vec{J}_I axes form the ground plane, while the \vec{K}_I axis completes the right-handed triad and points into the ground.

The ropes (drag rope, dump rope, and hoist rope) and chains (left drag chain, left lower hoist chain, left upper hoist chain, right drag chain, right lower hoist chain, and right upper hoist chain) are dynamically modeled in the same manner. In this paper, all ropes and chains are called “rope segments”. Differences in dynamic characteristics are realized through appropriate physical properties for a particular rope or chain. The rope segments of the dragline excavator system couple the various system components together. The motion of the end-points of a rope segment largely influences the dynamic behavior of the rope segment as a whole. For a rope segment, each edge is associated with either the beginning or end of the rope segment. For example, the left lower hoist chain is connected to the bucket and the left side of the spreader bar. The connection with the bucket is defined as the beginning connection point, while the connection with the left lower hoist chain is defined as the ending connection. Some rope segments interact with a pulley in the middle of the rope segment. For example, the dump rope is connected to the hoist coupler pulley.

The bodies that constitute the dragline excavator system (bucket, spreader bar, hoist coupler, drag coupler) are linked together by rope segments. Generally, each body has several rope segments attached to it. The weight of the body and the forces and moments generated by the rope connections dictate the motion of the individual bodies. For example, the bucket has five rope segments connected to it, namely the left drag chain, the right drag chain, the left lower hoist chain, the right lower hoist chain, and the dump rope.

Each rope segment is dynamically modeled as a set of particles connected by springs and dampers. Thus, all the mass elements of the system, including all bodies (bucket, spreader bar, hoist coupler, and drag coupler) and all

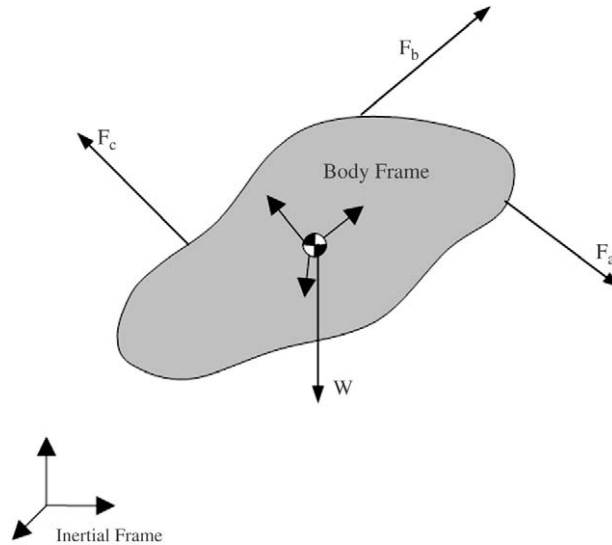


Fig. 3. Body dynamic model schematic.

particles on each rope segment (drag rope, dump rope, hoist rope, left drag chain, left lower hoist chain, left upper hoist chain, right drag chain, right lower hoist chain, and right upper hoist chain), are connected to other system mass elements by springs and dampers. Connection forces are simply treated as external forces acting on the body. Thus, derivatives of the state vector can be directly computed from the state vector in a straightforward manner.

2.1. Generic body equations of motion

The dynamic equations for all body elements assume the same structural form. This section develops the basic dynamic equations of motion used for any body element. Each body is modeled as being rigid and undergoes three-dimensional motion. Hence, 6 degrees of freedom or 12 state variables are required to describe the position and orientation of each rigid body at a given instant in time. The degrees of freedom for each body include three position components of the mass center of the body as well as three Euler orientation angles of the body. A schematic of a general rigid body of the system is shown as Fig. 3. The translational dynamics of the mass center of an arbitrary body are given by Eqs. (1) and (2):

$$\begin{Bmatrix} \dot{x}_B \\ \dot{y}_B \\ \dot{z}_B \end{Bmatrix} = \begin{Bmatrix} u_B \\ v_B \\ w_B \end{Bmatrix} \tag{1}$$

$$\begin{Bmatrix} \dot{u}_B \\ \dot{v}_B \\ \dot{w}_B \end{Bmatrix} = \begin{Bmatrix} X_B/m_B \\ Y_B/m_B \\ Z_B/m_B + g \end{Bmatrix} \tag{2}$$

In Eq. (2), m_B is the mass of the body and X_B, Y_B, Z_B are the components of the external rope coupling forces on the body expressed in the inertial reference frame. The orientation of a body element is defined by a sequence of three body fixed Euler angle rotations [9] shown in Fig. 4. Starting from the inertial reference frame, a rotation of θ_B is executed about the \vec{I}_I axis. The resulting rotated reference frame is called the O frame. Next, the O frame is rotated about the \vec{I}_O axis by the angle ϕ_B . The resulting reference frame is denoted the T frame. The T frame is subsequently rotated about the \vec{K}_T axis by the angle ψ_B , yielding the body reference frame. The angles ϕ_B, θ_B , and ψ_B are the Euler angles associated with the body. The kinematic relationship between time derivatives of the Euler angles and body frame angular velocity components is shown in Eq. (3):

$$\begin{Bmatrix} \dot{\phi}_B \\ \dot{\theta}_B \\ \dot{\psi}_B \end{Bmatrix} = \begin{bmatrix} c\psi_B & -s\psi_B & 0 \\ s\psi_B/c\phi_B & c\psi_B/c\phi_B & 0 \\ s\psi_B t\phi_B & c\psi_B t\phi_B & 1 \end{bmatrix} \begin{Bmatrix} p_B \\ q_B \\ r_B \end{Bmatrix} \tag{3}$$

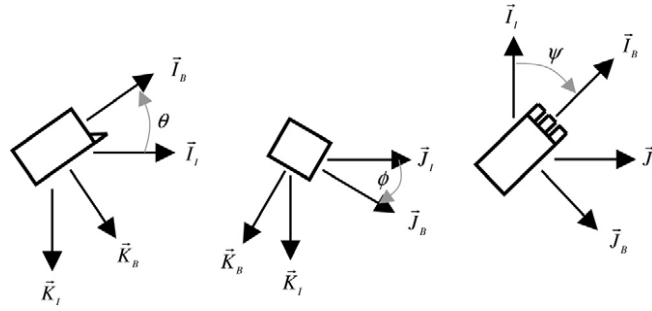
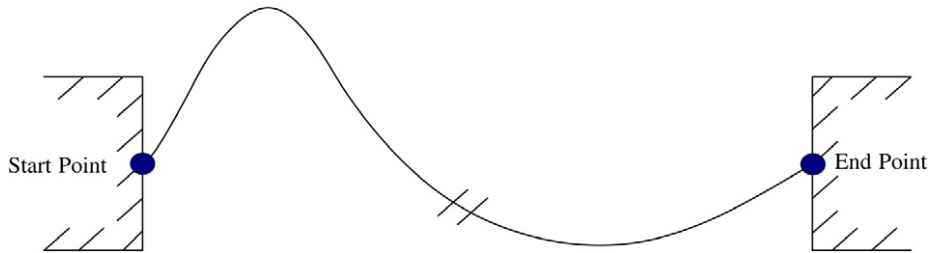
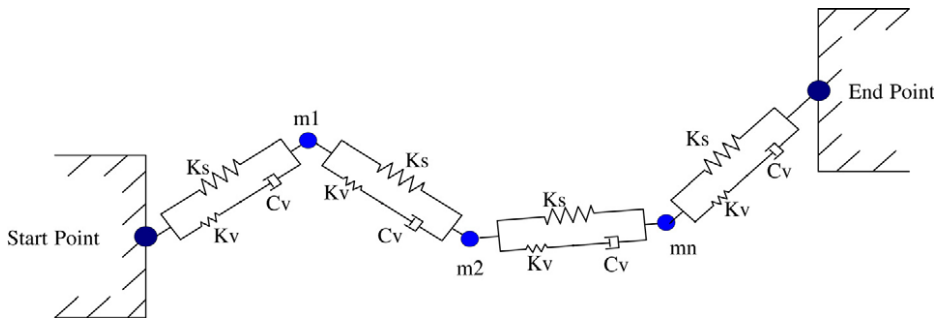


Fig. 4. Bucket Euler angle diagrams (each rotation shown with other angles zero).



a. Continuous rope segment.



b. Discrete rope segment.

Fig. 5. Rope dynamic model schematic.

Eq. (3) uses the following shorthand notation for trigonometric sine, cosine, and tangent functions: $s_\alpha \equiv \sin \alpha$, $c_\alpha \equiv \cos \alpha$, and $t_\alpha \equiv \tan \alpha$. The rotational dynamic equation for a body is given in Eq. (4):

$$\begin{Bmatrix} \dot{p}_B \\ \dot{q}_B \\ \dot{r}_B \end{Bmatrix} = [I_B]^{-1} \left[\begin{Bmatrix} L_B \\ M_B \\ N_B \end{Bmatrix} - \begin{bmatrix} 0 & -r_B & q_B \\ r_B & 0 & -p_B \\ -q_B & p_B & 0 \end{bmatrix} [I_B] \begin{Bmatrix} p_B \\ q_B \\ r_B \end{Bmatrix} \right] \quad (4)$$

In Eq. (4), I_B denotes the mass moment of inertia matrix of the body about its own mass center and L_B, M_B, N_B represent the components of the total externally applied moment vector on the body about its own mass center expressed in its own reference frame.

2.2. Generic rope segment equations of motion

The dynamic equations for all rope segments assume the same structural form. This section develops the basic dynamic equations of motion used for any rope segment. Fig. 5a depicts a typical rope segment consisting of a single length of rope with both ends attached to a moving body. Each rope segment is split into n_r particles and $n_r + 1$ elastic elements using truss finite elements. A standard linear solid visco-elastic element is used to connect particles.

Collectively, the motion of the particles defines the motion of the complete rope segment. Each particle on a rope segment is a point mass possessing three translation degrees of freedom. Forces that drive the motion of the particles include particle weight and adjacent visco-elastic element line forces. The dynamic equations for one particle on a rope segment are structurally the same for all particles, so the formulas to follow are shown only for the i th particle on an arbitrary rope segment:

$$\begin{Bmatrix} \dot{x}_{R_i} \\ \dot{y}_{R_i} \\ \dot{z}_{R_i} \end{Bmatrix} = \begin{Bmatrix} u_{R_i} \\ v_{R_i} \\ w_{R_i} \end{Bmatrix} \tag{5}$$

$$\begin{Bmatrix} \dot{u}_{R_i} \\ \dot{v}_{R_i} \\ \dot{w}_{R_i} \end{Bmatrix} = \frac{1}{m_{R_i}} \begin{Bmatrix} X_{T_i} - X_{T_{i+1}} \\ Y_{T_i} - Y_{T_{i+1}} \\ Z_{T_i} - Z_{T_{i+1}} \end{Bmatrix} + \begin{Bmatrix} 0 \\ 0 \\ g \end{Bmatrix} \tag{6}$$

In Eq. (6), m_{R_i} is the mass of the i th particle on a rope segment and g is the gravitational constant. The terms $X_{T_i}, Y_{T_i}, Z_{T_i}$ and $X_{T_{i+1}}, Y_{T_{i+1}}, Z_{T_{i+1}}$ represent the visco-elastic line force vector components expressed in the inertial reference frame of the line elements adjacent to the i th particle.

The line forces are caused by strain of the rope and are directed parallel to the line. Rope line flexibility generates resistive stiffness and damping forces caused by rope line segment extension and extension rate. In order to compute the visco-elastic line forces, it is useful to define a rope segment position and velocity difference vector for each rope segment. The difference vectors are formed by subtracting the position or velocity components of the $i + 1$ rope particle, or ending connection, from the i th rope particle component, or beginning connection. This results in $n_r + 1$ difference vectors for each rope. The terms $\Delta x_{R_i}, \Delta y_{R_i}$, and Δz_{R_i} represent the components of the position difference vectors, while the velocity difference vectors are used to construct the stretch rate, s_{R_i} . Using the rope segment position difference and velocity difference data, an expression for the elastic line force can be formed directly:

$$\begin{Bmatrix} X_{R_i} \\ Y_{R_i} \\ Z_{R_i} \end{Bmatrix} = \frac{F_{R_i}}{\sqrt{\Delta x_{R_i}^2 + \Delta y_{R_i}^2 + \Delta z_{R_i}^2}} \begin{Bmatrix} \Delta x_{R_i} \\ \Delta y_{R_i} \\ \Delta z_{R_i} \end{Bmatrix} \tag{7}$$

Eqs. (8) and (9) provide expressions for the elastic line force, F_{R_i} , in terms of the strain and strain rate of the visco-elastic line element:

$$F_{R_i} \dot{\bullet} + \frac{K_{vR_i}}{C_{vR_i}} F_{R_i} = \begin{cases} (K_{vR_i} + K_{sR_i}) \dot{s}_{R_i} + \frac{K_{vR_i} K_{sR_i}}{C_{vR_i}} s_{R_i}, & s_{R_i} - L_{R_i} > 0 \\ 0, & s_{R_i} - L_{R_i} \leq 0 \end{cases} \tag{8}$$

$$s_{R_i} = \sqrt{\Delta x_{R_i}^2 + \Delta y_{R_i}^2 + \Delta z_{R_i}^2} \tag{9}$$

In Eq. (8), K_{vR_i}, C_{vR_i} and K_{sR_i} are the viscous stiffness, viscous damping, and static stiffness coefficients respectively, for an individual visco-elastic line element. Also, L_{R_i} is the nominal unstretched line length of an individual line element. All individual line elements for a given rope segment have the same static and viscous stiffness coefficients, viscous damping coefficient, and unstretched line length. The first condition in Eq. (8) represents the normal tension condition between two adjacent particles. In this case, the distance between the two adjacent particles is greater than the unstretched elastic line element length, and a nonzero tension force in the line persists. The second condition in Eq. (8) is the slack condition. It stipulates that, when the unstretched elastic line element length is greater than the distance between two adjacent particles, the elastic force is zero.

The number of state variables required to model a rope segment can be large. Consider a rope segment split into 20 particles. Since each particle requires six state variables and each segment requires an additional state variable, this rope segment would require a total of 141 state variables to define the motion of the complete rope segment. As the number of beads used to represent each rope and chain is increased, the simulation model converges to the measured position. A balance between the accuracy of the model and number of states must be selected by the analyst.

2.3. Rope edge point position and velocity

Edge point position and velocity of a rope segment is required for visco-elastic line force computation. For edge points of a rope segment that are fixed on a body of the system, expressions for the position and velocity are formed from the motion of the connection point on the body. The inertial position vector components of the connection of a rope segment and a body is constructed as the distance from the inertial reference frame to the mass center of the body plus the distance vector from the body mass center to the connection point:

$$\begin{Bmatrix} x_C \\ y_C \\ z_C \end{Bmatrix} = \begin{Bmatrix} x_B \\ y_B \\ z_B \end{Bmatrix} + [T_{B \rightarrow I}] \begin{Bmatrix} SL_C^B - SL_B \\ BL_C^B - BL_B \\ WL_C^B - WL_B \end{Bmatrix} \quad (10)$$

The components x_C, y_C, z_C in Eq. (10) represent the inertial position components of a rope segment and body interface. The inertial location of the mass center of the body is denoted as x_B, y_B, z_B . The second term in Eq. (10) is the inertial position vector components of the distance from the mass center of the body to the interface point. The matrix $T_{B \rightarrow I}$ is an orthonormal transformation relating the body reference frame to the inertial reference frame:

$$T_{B \rightarrow I} = \begin{bmatrix} c\psi_B c\theta_B + s\psi_B s\phi_B s\theta_B & -s\psi_B c\theta_B + c\psi_B s\phi_B s\theta_B & c\phi_B s\theta_B \\ s\psi_B c\phi_B & c\psi_B c\phi_B & -s\phi_B \\ -c\psi_B s\theta_B + s\psi_B s\phi_B c\theta_B & s\psi_B s\theta_B + c\psi_B s\phi_B c\theta_B & c\phi_B c\theta_B \end{bmatrix} \quad (11)$$

The components SL_C^B, BL_C^B, WL_C^B are the body frame coordinates of the interface point, while the components SL_B, BL_B, WL_B are the body frame coordinates of the body mass center. The velocity of the interface point with respect to inertial space is obtained by differentiating Eq. (10).

Some rope segment edge points are not connected to bodies included in the dynamic system. For example, the end-point of the hoist rope is connected to the hoist reel. For end-points not attached to a body element of the system, the motion of the connection point is known as a function of time. Prior specification of an excavation maneuver defines the inertial position and velocity of the hoist reel, drag reel, and boom points. Furthermore, definition of an excavator maneuver also yields the length of line of the hoist and drag reels as a function of time. Computationally, any prescribed motion variables are determined by linear interpolation of a table of data with time as the abscissa and the prescribed motion parameter as the ordinate.

2.4. Body forces and moments

The forces and moments acting on a body of the dragline excavation system consist of body weight and elastic line forces from rope segments connected to the body. Each rope segment is divided into n_r particles and $n_r + 1$ adjoining elastic elements. The visco-elastic forces applied to a body are generated from either the first or last elements, depending on whether the connection is a beginning or ending connection point for the rope segment. Beginning connections use the first line element force of a rope segment, while ending connections use the last line element force of a rope segment:

$$\begin{Bmatrix} X_B \\ Y_B \\ Z_B \end{Bmatrix} = \sum_{j=1}^{n_c} a_j \begin{Bmatrix} X_{T_{e_j}} \\ Y_{T_{e_j}} \\ Z_{T_{e_j}} \end{Bmatrix} \quad (12)$$

In Eq. (12), the index e_j is either 1 or $n_r + 1$, depending on whether the j th rope segment connection is a beginning or ending connection. When the connection is a beginning connection, $a_j = -1$; when the connection is an ending connection, $a_j = 1$. The moment about the mass center of a body due to the connection forces shown above is computed as a cross-product of the distance vector from the mass center to the connection location and the connection force. Both the distance vector and the connection forces are expressed in the body reference frame, so the resulting moments are also expressed in the body reference frame as required in the equations of motion:

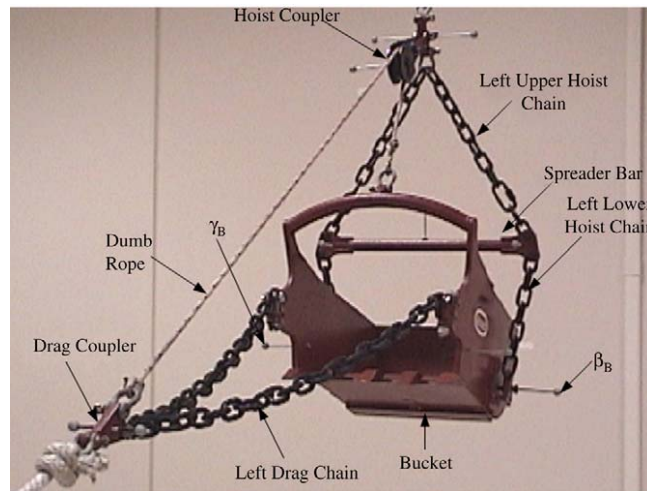


Fig. 6. 1/16-scale dragline excavator rigging.

$$\begin{Bmatrix} L_B \\ M_B \\ N_B \end{Bmatrix} = \sum_{j=1}^c a_j [S_{C_j}] [T_{B \rightarrow I}]^T \begin{Bmatrix} X_{T_{e_j}} \\ Y_{T_{e_j}} \\ Z_{T_{e_j}} \end{Bmatrix} \quad (13)$$

In Eq. (13), S_{C_j} is a matrix cross-product operator.

2.5. Pulley modeling

The dragline excavation system utilizes pulleys in rigging various ropes. The boom pulley is attached to the boom and located at the top of the boom. It interfaces with the hoist rope and directs the hoist rope upward from the hoist coupler and then downward to the hoist rope reel on the excavator body. The hoist coupler pulley guides the dump rope from the bucket to the drag coupler. For the purposes of dynamic modeling, pulleys serve to change the position of a rope segment by enforcing a constraint that part of the rope segment must lie on the pulley. Each pulley is modeled as a small ring through which a rope segment passes. The tension in the elastic line segment exerts a force on the body that the pulley is connected.

3. Dragline excavation system motion measurement system

A 1/16-scale dragline excavator system is the basic system examined. Motion of various bodies, ropes, and chains are measured with a three-dimensional optical motion capture system. The finite capture volume of the optical system covers a majority of the operating range of the 1/16-scale excavator system.

3.1. Test platform

As shown in Fig. 6, the scaled dragline excavator system consists of four rigid bodies: the bucket, spreader bar, hoist cluster, and drag cluster. The bucket is approximately 203 mm wide by 381 mm long by 152 mm tall and weighs just over 54 N. Weights, inertial properties and center-of-mass location for each body are listed in Table 1. The scaled dragline excavator system also employs three ropes (drag, dump and hoist ropes), and six chains (left drag chain, left lower hoist chain, left upper hoist chain, right drag chain, right lower hoist chain, and right upper hoist chain). Both the drag and hoist lines are half-inch rope, the dump line is quarter-inch rope, and all chains are 9.5 mm closed-link chain. Chain and rope properties, including mass, length, static and viscous spring constants, and viscous damping coefficients, are listed in Table 2. Chain and rope spring constants and damping coefficients are found by directly measuring the static spring stiffness K_s ; the visco-elastic stiffness and damping coefficients are then determined by an iterative process of comparing and matching measured and simulated rope data.

Table 1
Physical properties of bodies

Parameter	Bucket	Drag cluster	Hoist cluster	Spreader bar
Mass, m_B (kg)	5.4975	0.0876	0.3692	0.3900
C.G. location, SL_B (m)	0.0933	0.0	0.0	0.0
C.G. location, BL_B (m)	0.0	0.0	0.0	0.0
C.G. location, WL_B (m)	-0.0207	0.0	0.0	0.0
Inertia, $I_{B_{XX}}$ (kg m^2)	0.0712414	0.0000068	0.0000678	0.0059656
Inertia, $I_{B_{YY}}$ (kg m^2)	0.0858639	0.0000298	0.0007728	0.0000502
Inertia, $I_{B_{ZZ}}$ (kg m^2)	0.0119312	0.0000244	0.0007321	0.0059385

Table 2
Physical properties of ropes

Rope segment	Number of particles	Rope length (m)	Rope mass (N/m)	Static stiffness ((N/m)/m)	Viscous stiffness ((N/m)/m)	Viscous damping ((N/(m/s))/m)
Drag rope	6	1.829	0.06751	1,859	7439	74
Dump rope	5	1.088	0.07278	3,513	5269	53
Hoist rope	12	3.658	0.06751	1,859	7439	74
Left drag chain	4	0.610	0.55781	24,795	2755	14
Left lower hoist chain	2	0.183	0.55781	24,795	2755	14
Left upper hoist chain	3	0.305	0.55781	24,795	2755	14

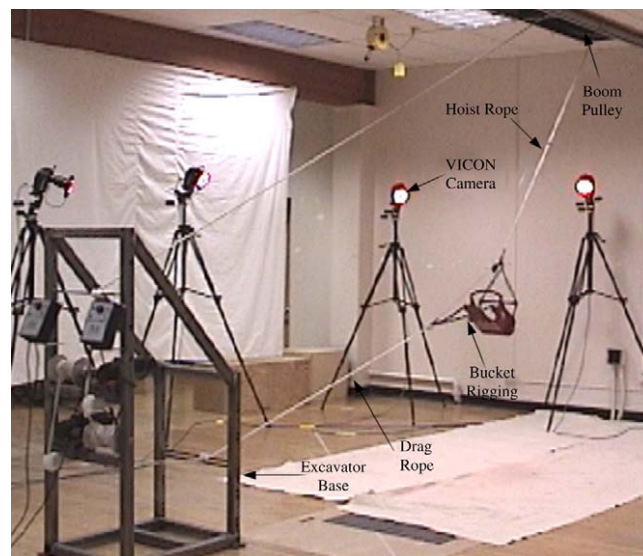


Fig. 7. 1/16-scale dragline excavator system.

The excavator is composed of two separate structures: the boom pulley, which is mounted to the wall with a square tube steel cantilever beam; and the excavator base, which is a 0.9 m by 0.9 m by 1.5 m steel frame vibration-isolated and anchored to the floor opposite the boom pulley. The assembled system is shown in Fig. 7. The wall-mounted boom pulley functions as both the boom and the boom pulley from Fig. 1. The excavator base provides a platform for mounting drag and hoist reels. When assembled, the 1/16-scale dragline excavator system spans 4 m high by 5.7 m long, allowing the bucket to operate in a 10.8 m² area.

The drag and hoist reel systems are both composed of a rope spool, direct current motor, motor controller, and two rope sheaves. The first sheave directs the rope onto the center of the reel, while the second sheave centers the rope on the excavator base and defines the location of the reel. Drag and hoist rope windup and payout are controlled by an operator positioned behind the excavator base. Rope speeds vary from ± 1.3 m/s.

3.2. Instrumentation

The position of each body and a portion of the drag and hoist ropes is tracked using a 3-D optical position analysis system from VICON Motion Systems [10]. Spherical reflective markers, 5 mm in diameter, are placed on each body of interest. As shown in Fig. 7, six cameras strategically placed throughout the laboratory emit and collect visible red light reflected from the markers. Using optical correlation techniques, the position of the center of each marker is determined in three dimensions. This data is time stamped and stored in a text file, which is then used to determine drag and hoist rope lengths, along with body position, velocity, orientation, and rotational velocities.

As shown in Fig. 6, mounting rods are fixed to each of the four system bodies to extend the markers away from the body to reduce occlusion. Four markers are mounted to the bucket: two on either side of the lower hoist chain mount and two on each side of the bucket nose. Three markers are mounted to the hoist cluster: one extended from the pulley center, and one on either side of the hoist cluster base. Three markers are mounted to the spreader bar: one is directed upwards from the cross bar, and one from both the left and right lower hoist chain mount points. The drag cluster has only two markers extended from either side of the mass center. Three markers on a body define a plane which is used to determine position and orientation data of the body. Two markers on a body define a single axis, which is used to determine only position data of the body.

As shown in Fig. 7, a circle of visible red diodes is fixed around each camera lens. A filter inside the camera detects the visible red light reflected from the markers, capturing a two-dimensional picture of the camera view. Data from all six cameras are collected and used to determine the three-dimensional position of all visible markers. Each camera has 1.2 Mega-pixel resolution and is capable of capturing marker position at a rate of 1000 Hz. Marker position is determined within 1 mm at slower sample rates up to 200 Hz. The camera system is calibrated by first defining a right-hand coordinate system with four static markers in the x - y plane. Next, two markers fixed a known distance apart are passed throughout the entire capture area, allowing the system to determine the position of each camera in the previously defined coordinate system. The marker position for subsequent captures is then determined in this coordinate system.

3.3. Data processing

Data collected by the motion capture system is used to determine the position and orientation of the bucket, spreader bar, hoist cluster, and drag cluster, along with the lengths of the drag and hoist ropes. Position and orientation data are numerically differentiated using second-order finite differences to obtain linear and angular velocities for each body. A running average with a 12-sample window size is implemented to reduce noise amplification.

To generate the mass center position and orientation of a body, first, marker position data are processed to generate the transformation matrix from the local body frame to the ground frame. To illustrate this procedure, consider the bucket that has four markers rigidly attached. These marker points are denoted as α_B , β_B , γ_B and δ_B . The unit vectors that define the bucket body frame are defined such that the \vec{J}_B axis is directed laterally. The \vec{I}_B axis points forward out of the front of the bucket and the \vec{K}_B axis points down through the bottom of the bucket. The four bucket markers shown in Fig. 6 are used to define the bucket body frame in a detailed manner using the equations below:

$$\vec{J}_B = \frac{\vec{r}_{O \rightarrow \beta_B} - \vec{r}_{O \rightarrow \alpha_B}}{\|\vec{r}_{O \rightarrow \beta_B} - \vec{r}_{O \rightarrow \alpha_B}\|} = j_{BX} \vec{I}_I + j_{BY} \vec{J}_I + j_{BZ} \vec{K}_I \tag{14}$$

$$\vec{K}_B = \frac{(\vec{r}_{O \rightarrow \gamma_B} - \vec{r}_{O \rightarrow \alpha_B}) \times \vec{J}_B}{\|(\vec{r}_{O \rightarrow \gamma_B} - \vec{r}_{O \rightarrow \alpha_B}) \times \vec{J}_B\|} = k_{BX} \vec{I}_I + k_{BY} \vec{J}_I + k_{BZ} \vec{K}_I \tag{15}$$

$$\vec{I}_B = \frac{\vec{J}_B \times \vec{K}_B}{\|\vec{J}_B \times \vec{K}_B\|} = i_{BX} \vec{I}_I + i_{BY} \vec{J}_I + i_{BZ} \vec{K}_I \tag{16}$$

Since the bucket frame and inertial frame unit vectors are related by

$$\begin{Bmatrix} \vec{I}_B \\ \vec{J}_B \\ \vec{K}_B \end{Bmatrix} = T_{B \rightarrow I}^T \begin{Bmatrix} \vec{I}_I \\ \vec{J}_I \\ \vec{K}_I \end{Bmatrix} \tag{17}$$

equating components resolved in the inertial frame yields:

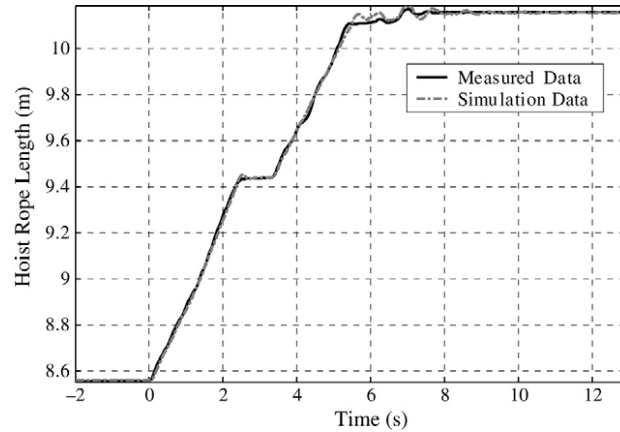


Fig. 8. Measured and predicted hoist rope length vs. time.

$$\begin{bmatrix} i_{BX} & j_{BX} & k_{BX} \\ i_{BY} & j_{BY} & k_{BY} \\ i_{BZ} & j_{BZ} & k_{BZ} \end{bmatrix} = T_{B \rightarrow I}^T \begin{bmatrix} 1 & 0 & 0 \\ 0 & 1 & 0 \\ 0 & 0 & 1 \end{bmatrix} \quad (18)$$

The position vector from the ground reference frame to the bucket reference frame is computed as a linear combination of the bucket marker points. From basic geometric data, the distance vector from the bucket reference frame to the bucket mass center is known. Thus the position vector from the ground reference frame to the bucket mass center is computed as a superposition of these two vectors, expressing both vectors in the ground reference frame. The distance vector from the bucket reference frame to the bucket mass center is expressed in inertial coordinates with the help of the transformation matrix defined in Eq. (18).

The Euler orientation angles of the bucket are obtained by comparing the functional form of the transformation matrix in Eq. (14) with the measured transformation matrix in Eq. (18), yielding

$$\phi_B = \sin^{-1}(-j_{BZ}) \quad (19)$$

$$\theta_B = \sin^{-1}\left(\frac{i_{BZ}}{\cos(\phi_B)}\right) \quad (20)$$

$$\psi_B = \sin^{-1}\left(\frac{j_{BX}}{\cos(\phi_B)}\right) \quad (21)$$

Drag and hoist rope lengths are determined by fitting a cubic polynomial in the x - z plane to the rope marker positions:

$$z_i = a_0 + a_1x_i + a_2x_i^2 + a_3x_i^3 + e \quad (22)$$

In Eq. (22), e is the residual and a_0 , a_1 , a_2 , and a_3 are unknown coefficients.

4. Dig maneuver results

A dig maneuver begins with the hoist rope set at 8.6 m and the drag rope at 4.2 m. This places the bucket 1.2 m above the dig plane and near the end of the excavator's travel in the longitudinal direction with a negative pitch angle of 52° . At $t = 0$, the bucket is swept down and towards the operator by lengthening the hoist rope at 0.36 m/s while reeling in the drag rope at 0.30 m/s. The hoist rope is then stopped for 1 s, while the drag rope pulls the bucket along in the longitudinal direction at 0.61 m/s. While continually reeling the drag line in, the hoist line is again paid out at 0.30 m/s for another 2 s. The hoist line is then stopped, while the drag line continues for 1 s more, after which both reels are stopped. The dig maneuver ends with the hoist rope set at 10.1 m and the drag rope at 1.4 m, placing the bucket 0.70 m above the dig plane near the middle of the system's longitudinal travel. Hoist and drag rope lengths are plotted against time in Figs. 8 and 9.

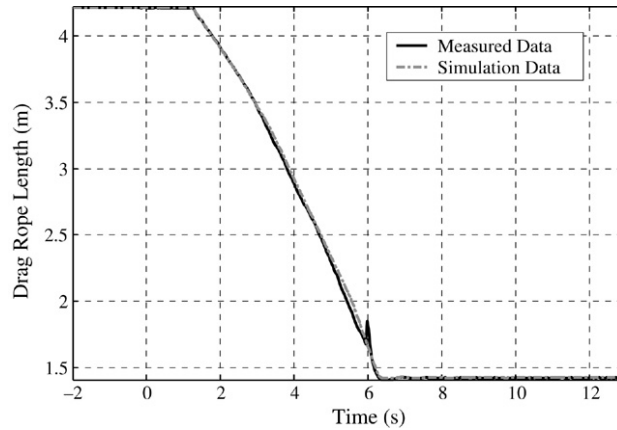


Fig. 9. Measured and predicted drag rope length vs. time.

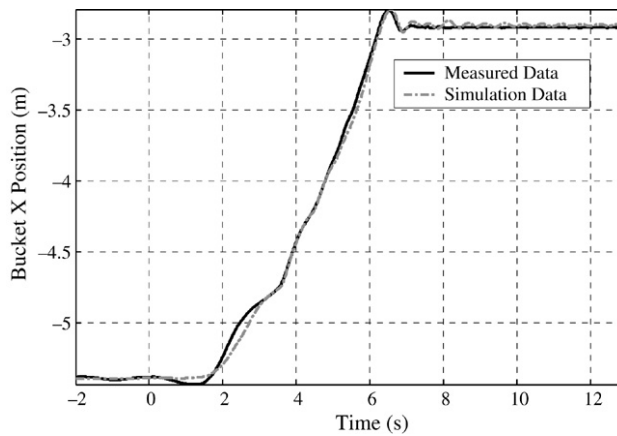


Fig. 10. Measured and predicted X inertial position of bucket mass center vs. time.

The bucket position begins and ends with a slight shift between measured and predicted values, while pitch differs by two to four degrees. The position in the \vec{I}_I and \vec{K}_I directions and the pitch angle for the dig maneuver are plotted in Figs. 10 through 12. Note that predicted and measured bucket position match closely in all directions throughout the entire dig maneuver. The predicted motion tends to oscillate slightly more in all cases, yet location and frequency match well. The predicted values of bucket Euler pitch angle tend to oscillate more and with larger amplitude than measured values. Bucket position in the \vec{J}_I direction, bucket roll and yaw angles are all nearly zero for both measured and simulated maneuvers.

The velocity in the \vec{I}_I and \vec{K}_I directions and the pitch rate of the bucket for the dig maneuver are plotted in Figs. 13 through 15. Translational velocities correlate well throughout the entire maneuver. The maximum measured longitudinal velocity is 0.99 m/s, occurring at 6.2 s, while the maximum predicted longitudinal velocity is 1.01 m/s and occurs at 5.95 s. The maximum measured vertical velocity is 0.73 m/s, occurring at 6.05 s, while the maximum predicted vertical velocity is 0.91 m/s and occurs at 6.27 s. The predicted bucket pitch rate is larger than the measured values throughout most of the maneuver. The maximum measured pitch rate of -2.4 rad/s occurs at 6.77 s, while the maximum predicted pitch rate of -3.2 rad/s occurs at 6.77 s.

The spreader bar and hoist cluster position in the longitudinal and vertical directions, along with Euler pitch angle, are compared during the maneuver in Figs. 16 through 19. The positions of the drag cluster in the longitudinal and vertical directions are compared in Fig. 20. The predicted spreader bar position in the longitudinal direction matches the measured position through the entire maneuver with a consistent offset of approximately 51 mm. In the vertical direction, predicted and measured motion match well until the end of the maneuver, where the measured position settles more quickly than predicted. The spreader bar’s measured pitch also tends to settle more quickly than predicted.

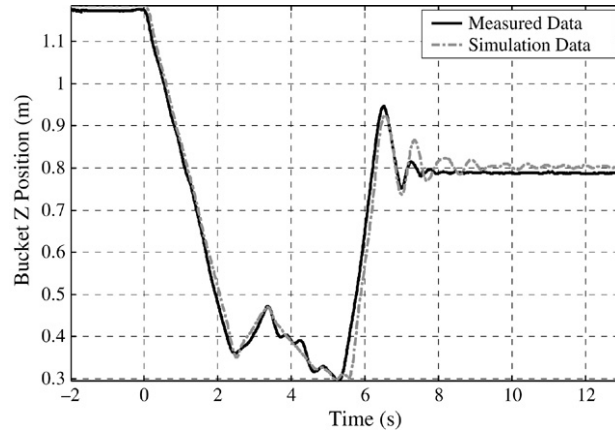


Fig. 11. Measured and predicted Z inertial position of bucket mass center vs. time.

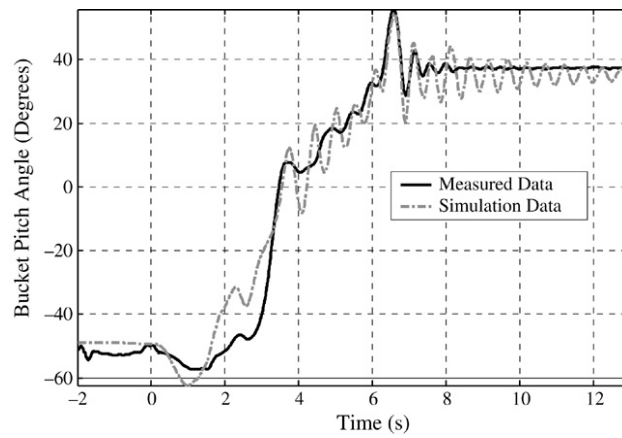


Fig. 12. Measured and predicted bucket pitch angle vs. time.

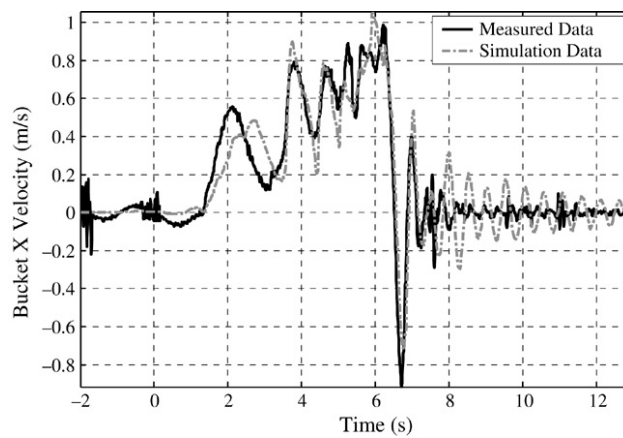


Fig. 13. Measured and predicted X inertial velocity of bucket mass center vs. time.

Similarly to the spreader bar and bucket, the hoist and drag clusters' predicted and measured motions match well through the entire maneuver, yet the measured motion tends to settle faster than predicted motion in the vertical direction and pitch angle.

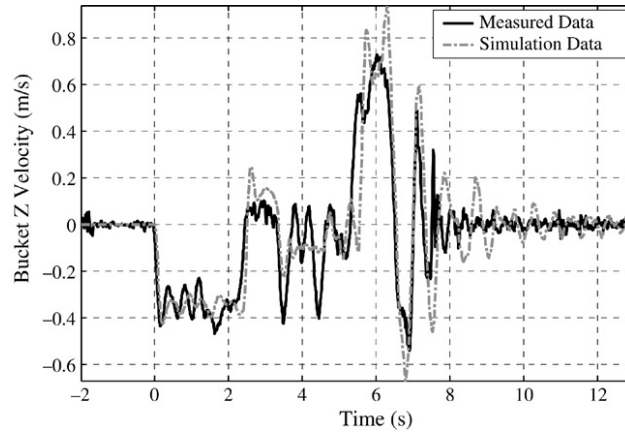


Fig. 14. Measured and predicted Z inertial velocity of bucket mass center vs. time.

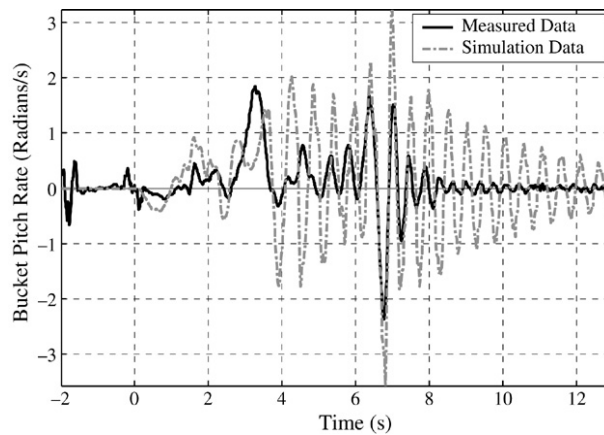
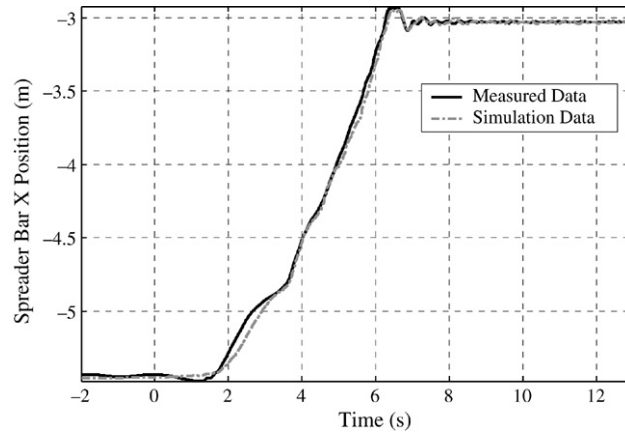


Fig. 15. Measured and predicted bucket pitch rate vs. time.

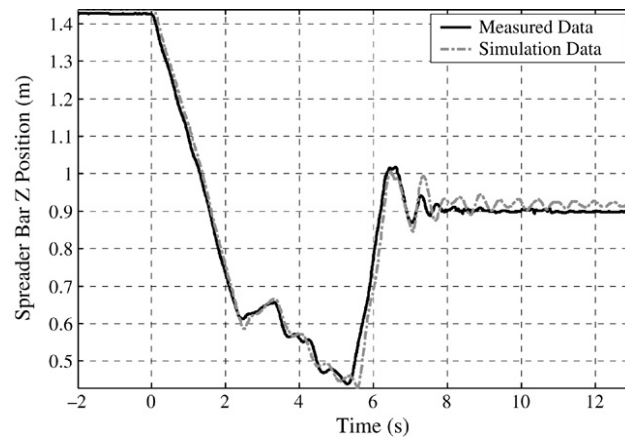
The only significant difference between predicted and measured motion throughout the dig maneuver is in the pitch dynamics of the bucket and hoist cluster, and the effects that this motion has on the system. These differences can mainly be attributed to un-modeled sources of damping in the system, including friction in the chain links, torsion damping in the ropes, rope bending damping, pulley friction, and pulley rotational momentum. Differences between predicted and measured positions and orientations are attributed to: the simple hoist cluster pulley model, which plays a large role in the pitch dynamics of the bucket; un-modeled rigging interactions such as rope and chain attachment moments, as well as rope and chain collisions; and system measurement errors.

4.1. Rope discretization

As previously mentioned, each rope segment is split into n_r particles and $n_r + 1$ elastic elements using truss finite elements. Collectively, the motion of the particles defines the motion of the complete rope segment. The effect of the discretization level of each rope on the simulation predictions is investigated at four levels of discretization tabulated in Table 3. Bucket pitch angle is compared against measured values for each bead discretization level in Fig. 21, where the baseline case is used for the motion comparisons (Table 2). Simulated pitch angle approaches measured the pitch angle as the discretization level is increased. The penalty associated with increasing the bead count is an increase in system states.



a. Measured and predicted X inertial position of spreader bar mass center vs. time.



b. Measured and predicted Z inertial position of spreader bar mass center vs. time.

Fig. 16. Measured and predicted position of spreader bar mass center vs. time.

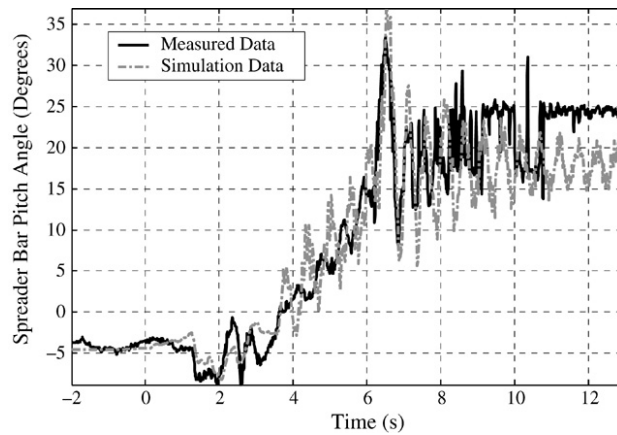
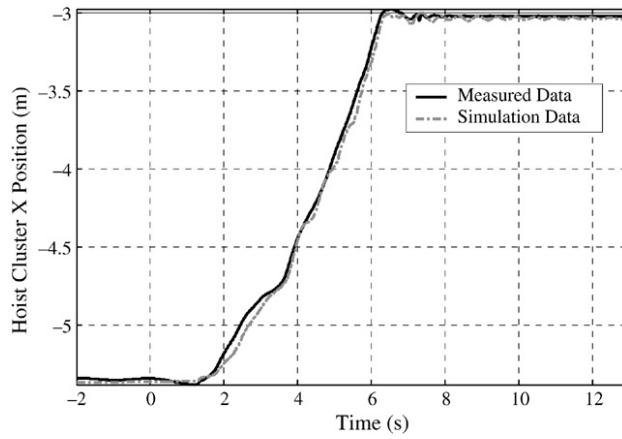
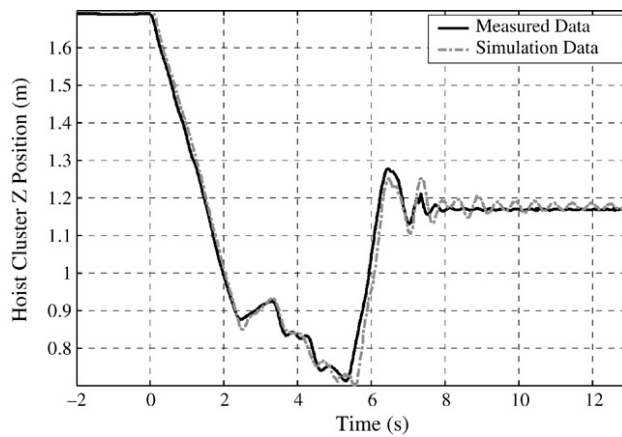


Fig. 17. Measured and predicted spreader bar pitch angle vs. time.



a. Measured and predicted X inertial position of hoist cluster mass center vs. time.



b. Measured and predicted Z inertial position of hoist cluster mass center vs. time.

Fig. 18. Measured and predicted position of hoist cluster mass center vs. time.

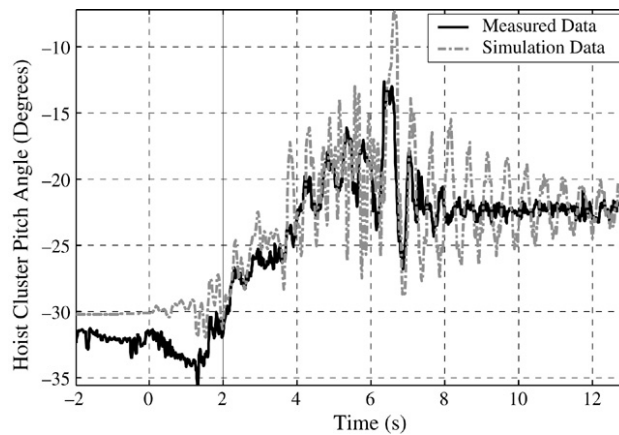
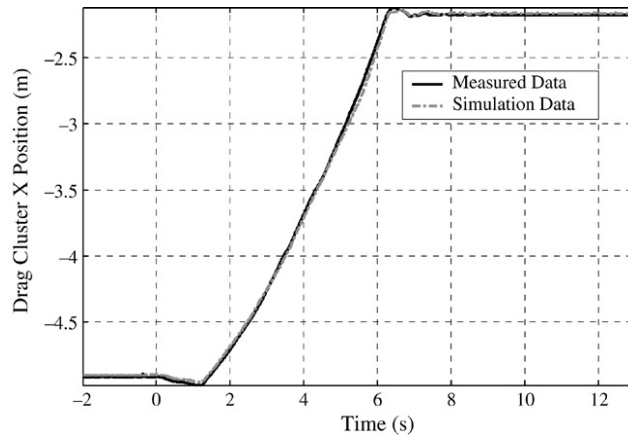
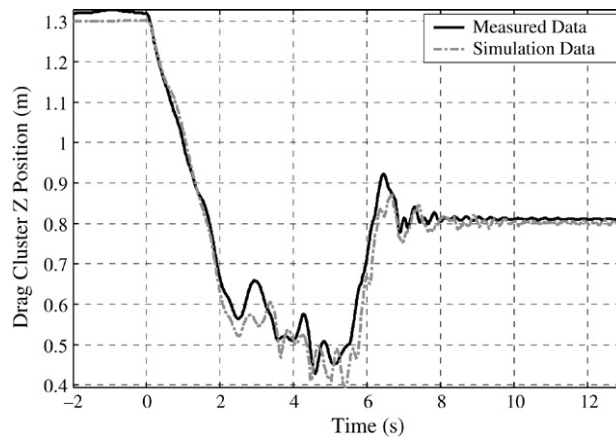


Fig. 19. Measured and predicted hoist cluster pitch angle vs. time.



a. Measured and predicted X inertial position of drag cluster mass center vs. time.



b. Measured and predicted Z inertial position of drag cluster mass center vs. time.

Fig. 20. Measured and predicted position of drag cluster mass center vs. time.

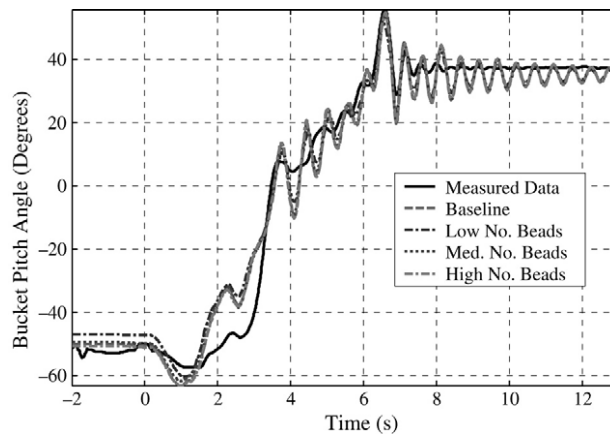


Fig. 21. Measured and predicted bucket pitch angle vs. time for varying bead discretization.

Table 3
Rope bead discretization level

Discretization level	Drag rope	Dump rope	Hoist rope	Left drag chain	Left lower hoist chain	Left upper hoist chain	Total # of rope states
Low	4	3	8	2	1	1	133
Base line	6	5	12	4	2	3	224
Medium	8	7	16	8	3	4	322
High	14	12	28	13	4	6	539

5. Conclusions

The work reported here focused on a detailed comparison of measured longitudinal motion of a scaled dragline excavation system with results generated by a complex dynamic simulation. Measured and predicted motions during a dig maneuver agrees favorably. System dynamics are also predicted well, with the exception of bucket and hoist cluster pitch dynamics. The primary difference between measured and predicted motions are relatively high-frequency, slowly decaying oscillations exhibited by simulation results. These differences can be attributed mainly to un-modeled sources of damping in the system, including friction in the chain links, torsion damping in the ropes, rope bending damping, pulley friction, and pulley rotational momentum.

References

- [1] C.E. McCoy, J.L. Crowgey, Anti-Tightline Control System for Draglines used in the Surface Mining Industry, IEEE, 1980, CH1575-0/80/0000-0140.
- [2] D.K. Haneman, H. Hayes, G.I. Lumley, Dragline performance evaluations for tarong coal using physical modeling, in: Third Large Open Pit Mining Conference, Mackay, 30 August–3 September 1992.
- [3] J.C. Rowlands, G.D. Just, Performance characteristics of dragline buckets, in: Third Large Open Pit Mining Conference, Mackay, 30 August–3 September 1992.
- [4] P.F. Knights, D.H. Shanks, Dragline productivity improvements through short-term monitoring, in: Institution of Engineers, Coal Handling and Utilization Conference, Sydney, 19–21 June 1990.
- [5] K. Pathak, K. Dasgupta, A. Chattopadhyay, Determination of the working zone of a dragline bucket, *Mining Technology* (February) (1992).
- [6] D.W. Hainsworth, P.I. Corke, G.J. Winstanley, Location of dragline bucket in space using machine vision techniques, in: *Speech and Signal Processing*, Adelaide, April 1994.
- [7] P.W. Cleary, The filling of dragline buckets, *Math. Engng. Ind.* 7 (1) (1998) 1–24.
- [8] P. Ridley, P. Corke, Calculation of dragline bucket pose under gravity loading, *Mechanism and Machine Theory* 35 (2000) 1431–1444.
- [9] J.H. Ginsberg, *Advanced Engineering Dynamics*, Cambridge University Press, New York, NY, 1995, pp. 119–162.
- [10] VICON Motion Systems Limited, *Vicon System Manual*, VICON 612, 12th edition, Lake Forest, CA, July 2002.